Valley-Selective Polarization in Twisted Bilayer Graphene Controlled by a Counter-Rotating Bicircular Laser Field

Jiayin Chen [1,2], **Candong Liu** [1,2,*] and **Ruxin Li** [1,2]

1   State Key Laboratory of High Field Laser Physics, Shanghai Institute of Optics and Fine Mechanics, Chinese Academy of Sciences, Shanghai 201800, China
2   Center of Materials Science and Optoelectronics Engineering, University of Chinese Academy of Sciences, Beijing 100049, China
*   Correspondence: cdliu@siom.ac.cn

Abstract: The electron valley pseudospin in two-dimensional hexagonal materials is a crucial degree of freedom for achieving their potential application in valleytronic devices. Here, bringing valleytronics to layered van der Waals materials, we theoretically investigate lightwave-controlled valley-selective excitation in twisted bilayer graphene (tBLG) with a large twist angle. It is demonstrated that the counter-rotating bicircular light field, consisting of a fundamental circularly-polarized pulse and its counter-rotating second harmonic, can manipulate the sub-cycle valley transport dynamics by controlling the relative phase between two colors. In comparison with monolayer graphene, the unique interlayer coupling of tBLG renders its valley selectivity highly sensitive to duration, leading to a noticeable valley asymmetry that is excited by single-cycle pulses. We also describe the distinct signatures of the valley pseudospin change in terms of observing the valley-selective circularly-polarized high-harmonic generation. The results show that the valley pseudospin dynamics can still leave visible fingerprints in the modulation of harmonic signals with a two-color relative phase. This work could assist experimental researchers in selecting the appropriate protocols and parameters to obtain ideal control and characterization of valley polarization in tBLG.

Keywords: valley pseudospin; twisted bilayer graphene; counter-rotating bicircular field

1. Introduction

It is a widely accepted fact that electrons possess two intrinsic degrees of freedom, namely, their charge and spin properties. In the last century, there has been significant advancement in conventional electronic components, primarily based on the manipulation of charge. However, several studies on magnetic nano-multilayer films and their magnetoresistance effects [1,2] have demonstrated the role of spin in information storage and transmission, thereby leading to the emergence of spintronics [3]. Furthermore, recent research has established that electrons in two-dimensional hexagonal materials possess an additional degree of freedom, known as the valley pseudospin, which corresponds to extreme points on the electron band dispersion curve. Such electrons are commonly found in materials such as graphene [4], layered transition metal dichalcogenides [5,6], and Weyl semimetal systems [7–9]. For instance, the energy band structure of graphene features two unequal yet degenerate Dirac points on the Fermi surface of the first Brillouin zone (BZ), referred to as the K_1 and K_2 valleys. Leveraging this novel quantum degree of freedom, valleytronics has emerged as a promising avenue for information encoding. In comparison with traditional electronic devices, the benefits of processing information with valleys include high integration, fast running speed, low energy consumption, and minimal information loss [10].

Valleytronics aims to manipulate the motion of electrons to induce valley polarization, a novel quantum degree of freedom that carries information and can be achieved by breaking spatial symmetry [11,12]. Over the past decade, significant progress has been made in

both theoretical and experimental studies on valley-related transport properties [13–15]. In addition, various optical-driven approaches have been proposed to achieve transient valley polarization [16–19]. Valley-selective excitation is governed by the resonance between the driving field and the energy bands. Therefore, precise sub-cycle control over the laser pulses provides new opportunities for valleytronics. However, there are several practical limitations and the short valley lifetimes ($10^3 \backsim 10^6$ fs) pose a significant challenge; thus, ultrafast valley polarization manipulation on the femtosecond timescale is an urgent need [20,21]. The lightwave-driven subcycle switching of the valley pseudospin in a tungsten diselenide monolayer opens the way for valley-selective control within several femtoseconds [22]. Recent theoretical works validate the feasibility of such ultrafast valley polarization manipulation [23–25]. The effect of optical excitation systems on valley polarization is also explored [11,26]; in particular, two-color circularly-polarized laser fields are demonstrated to contribute a robust mechanism for valley polarization [4,11]. Inversion symmetric materials, such as transition metal dichalcogenides bilayers and graphene, exhibit high degrees of valley polarization excited by few-cycle linearly polarized pulses [23]. The ultrafast valley switching in graphene [27], a typical Dirac material, has also been studied. Unlike dielectrics, the zero band gap property makes graphene exhibit an important interband transition, which can be intensively affected by intraband motion, especially under higher driving fields [28]. Owing to its high carrier mobility, electrical conductivity, and thermal/chemical stability, graphene is widely used and exhibits ideal properties in many fields, including quantum information [29], quantum dots [30], transport properties [31], and so on. It is worth mentioning that graphene can also be used to create various composites [32,33]. As another important Dirac material, tBLG receives significant attention due to its excellent electrical properties and application potentials in nanodevices. For example, tBLG possesses a unique Berry phase, translation symmetry, and periodicity of Moiré patterns, which make it totally different from monolayer graphene (MLG) [34]. Furthermore, tBLG has a high mobility [35], making it a suitable raw material for future high-speed electronic devices. However, similar to monolayer graphene, tBLG also has two unequal valleys. In addition, if the time inversion symmetry breaks spontaneously, tBLG enters a valley-polarized ground state [36]. To date, valley polarization induced by optical fields in pristine graphene has been partly investigated, while laser-induced valleytronics in tBLG has not been extensively discussed. The shorter spacing and more complex interference of the two valleys in tBLG may be detrimental to sharp valley asymmetry.

In this study, we investigate the valley asymmetry in tBLG with a large twisted angle. To induce valley-selective excitation, we employ a counter-rotating bicircular (CRB) light field that consists of a fundamental and counter-rotating frequency-doubled circularly-polarized pulse. The vector potential of the CRB field exhibits a specific trefoil pattern, and the relative orientation of vector potential to the lattice is controlled by a two-color phase, which is a key parameter. We present two typical vector potential patterns with different phases in Figure 1c,d, corresponding to the maximum excitation of the K_1 and K_2 valleys, respectively. The electron dynamics in tBLG is studied by solving the density matrix equation within the framework of the tight-binding approximation, with the basis vectors expanded in the Wannier gauge to avoid the problem of random phases of the dipole couplings [37]. We show that the valley asymmetry decreases with the increase in pulse duration, which is not observed in monolayer graphene. The underlying physical mechanism is elucidated by analyzing the evolution of the k-space total conduction band population over time. Additionally, the measurement of valley-selective polarization is achieved by harmonic characterization. Several characteristics, in addition to the two-color phase and duration, are briefly explored. Overall, this work provides a new insight into the control of valley dynamics in tBLG using the CRB field, and offers a promising avenue for the development of valleytronics based on tBLG.
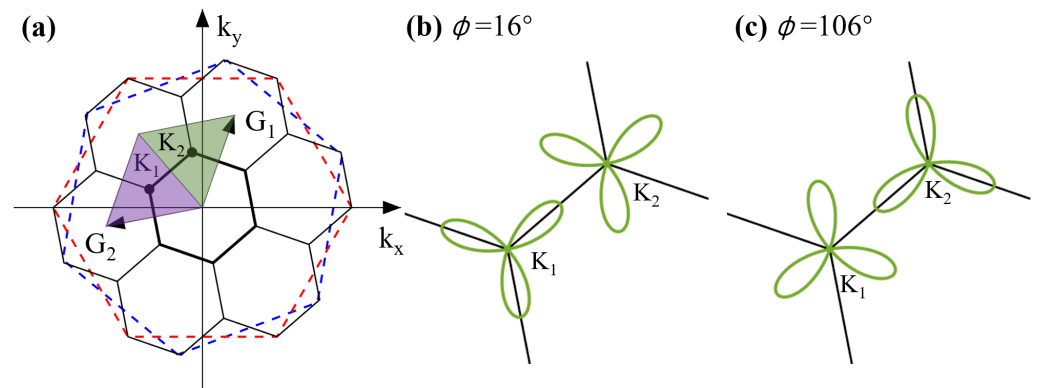
Figure 1. (**a**) The BZ of commensurate tBLG with a twisted angle $\theta \approx 21.8°$ ($m = 1$, $r = 1$). Starting from a perfect AB stacked, the first BZ of the top layer (blue-dashed hexagon) rotates $\theta \approx 21.8°$ counterclockwise relative to the first BZ of the bottom layer (red-dashed hexagon). The seven smaller black hexagons are the BZ of superlattice tBLG. $\mathbf{G}_1$ and $\mathbf{G}_2$ are the reciprocal lattice primitive vectors. The first BZ of tBLG is divided into $\mathbf{K}_1$ (purple shade) and $\mathbf{K}_2$ (green shade) valleys. (**b,c**) The relative position of CRB vector potential and Dirac points in reciprocal space, where two-color phase is set to (**b**) $\phi = 16°$ and (**c**) $\phi = 106°$ respectively.

2. Theoretical Method

We define the lattice structure of the tBLG by vertically stacking two MLG sheets together in an arbitrary orientation such that one of the layers is rotated by an angle θ with respect to the other layer. The interference of the two lattice periods results in the formation of a Moiré pattern, which can exist for any θ. However, a strictly periodic superstructure, characterized by the repetition of a large multiatomic supercell, only occurs for certain "commensurate" twist angles θ [38]. The commensurate rotation angle should satisfy [39–41]

$$\cos\theta = \frac{3m^2 + 3mr + r^2/2}{3m^2 + 3mr + r^2}, \tag{1}$$

where m and r are coprime positive integers. Here, θ represents the angle of rotation of the top layer, starting from an AB-stacked bilayer. The details of lattice structures are discussed in our previous work [42]. Among the superstructures with $\theta < 30°$, there is a special subset corresponding to $r = 1$, whereas the other commensurate superstructures with $r > 1$ can be seen as almost periodic repetitions of superstructures with $r = 1$ [34]. In this work, we focus on the commensurate structure given by $m = 1$ and $r = 1$, which corresponds to a twist angle $\theta \approx 21.8°$. This angle is large enough to cause significant inter-valley coupling, making it an ideal system to study the control mechanism of valley excitation in tBLG. Moreover, this configuration has the smallest supercell and requires the least computational power, making it an efficient system to study. For other twist angles, the tBLG manifests as either an incommensurate structure or a commensurate structure with a larger unit cell. The BZ of tBLG possessing the twist angle $\theta \approx 21.8°$ ($m = 1$ and $r = 1$) is displayed as the black bold hexagon region situated at the center of Figure 1a.

When it is subject to a laser field, the time-dependent Hamiltonian of tBLG can be expressed within the dipole approximation and in the length gauge. Specifically, the Hamiltonian takes the form:

$$H = H_0 + \mathbf{E}(t) \cdot \mathbf{r}, \tag{2}$$

where H_0 is the field-free Hamiltonian, $\mathbf{E}(t)$ is the electric field, and $\mathbf{r}$ is the position operator. To describe the quantum states of the electrons in the tBLG, we adopt the tight-binding model of Ref. [37]. The tight-binding parametrization is taken from Ref. [43]. Unless otherwise indicated, atomic units (a. u.) are used throughout: $e = \hbar = m_e = 1$,

where e and m_e are the electron charge and mass. The temporal evolution of the density matrix elements reads [37]

$$\frac{\partial \rho_{mn}(\mathbf{k}, t)}{\partial t} = -i[H_0(\mathbf{k}), \rho(\mathbf{k}, t)]_{mn} - i\mathbf{E}(t) \cdot [\mathbf{d}(\mathbf{k}), \rho(\mathbf{k}, t)]_{nm}, \quad (3)$$

where n and m are the band indexes, $\mathbf{d}(\mathbf{k})$ is the transition dipole moment, $\mathbf{k}(t) = \mathbf{k}_0 + \mathbf{A}(t)$ is the time-dependent momentum, $\mathbf{k}_0$ is the initial reciprocal coordinate, and $\mathbf{A}(t)$ is the vector potential. Only the p_z orbital of each carbon atom site is considered, and the intra-atomic dipole transition is forbidden. Hence, $\mathbf{d}(\mathbf{k})$ is zero in the calculation. After solving the density matrix equation, the current operator can be defined as [37]:

$$\mathbf{J} = -\sum_{\mathbf{k} \in BZ} \sum_{n,m} \left(\frac{\partial}{\partial \mathbf{k}} H_0(\mathbf{k}) \right) \rho_{mn}(\mathbf{k}, t). \quad (4)$$

The harmonic spectrum is calculated from the Fourier integral of the time derivative of current $\mathbf{J}(t)$. In the Bloch gauge, the diagonal terms of a density matrix represent the population of different bands at the end of the laser pulse. We assume that all valence bands in tBLG are initially occupied, and that the conduction bands are empty before excitation. These initial conditions can be easily linked to the Bloch density matrix. However, it is necessary to obtain the density matrix in the Wannier gauge by unitary transformation before evolution; it is obtained through unitary transformation from the Bloch representation as the initial conditions. The conversion between both gauges can be expressed in a set of unitary transformation [37]:

$$\rho_{mn}^{(H)}(\mathbf{k}, t) = \sum_{ab} U_{nb}^{\dagger}(\mathbf{k}) \rho_{ba}^{(W)}(\mathbf{k}, t) U_{am}(\mathbf{k}), \quad (5)$$

$$\rho_{mn}^{(W)}(\mathbf{k}, t) = \sum_{ab} U_{nb}(\mathbf{k}) \rho_{ba}^{(H)}(\mathbf{k}, t) U_{am}^{\dagger}(\mathbf{k}), \quad (6)$$

where $U(\mathbf{k})$ is a unitary matrix that diagonalizes $H_0^W(\mathbf{k})$. The superscript (H) denotes the Hamiltonian gauge, and (W) denotes the Wannier gauge. The representation of the density matrix element is determined by the type of base vector, while the density matrix Equation (3) does not depend on gauge.

Considering the electron–electron or electron–phonon scattering beyond the mean-field approximation, a dephasing process is introduced for a proper model. Thus, we define the dephasing time T_2 and give the relaxation term as the product of the nondiagonal element and $\exp(-\frac{\Delta t}{T_2})$ in the Hamiltonian gauge. Due to the fact that the dephasing process describes the exponential decay of interband polarization, the relaxation term cannot be directly added to Equation (3), thus acting on $\rho_{nm}^{(H)}(\mathbf{k}, t)$ rather than $\rho_{nm}^{(W)}(\mathbf{k}, t)$. Therefore, the dephasing mechanism is described as follows: At each evolution step of solving Equation (3) with the time interval Δt, $\rho_{nm}^{(W)}(\mathbf{k}, t)$ is transformed to $\rho_{nm}^{(H)}(\mathbf{k}, t)$ via Equation (5), followed by multiplying the off-diagonal element $\rho_{nm}^{(H)}(\mathbf{k}, t)$ by $\exp(-\frac{\Delta t}{T_2})$, and finally transformed back to $\rho_{nm}^{(W)}(\mathbf{k}, t)$ via Equation (6). The above procedure is repeated until the end of the dynamics evolution. The dephasing time $T_2 = 20$ fs is set throughout this study, and our simulation results are verified to be insensitive to dephasing time.

We consider the first BZ spanned by the primitive reciprocal vectors, and sample $\mathbf{k}$ points using a uniform grid spacing along two nonorthogonal directions, denoted by $\mathbf{G_1}$ and $\mathbf{G_2}$. The reciprocal space is sampled with a 400×400 grid, which is deemed sufficient for describing the valley polarization. The evolution time step is initially set to $\delta t = 0.2$ a.u.. The density matrix equation is numerically solved for each independent $\mathbf{k}$ by utilizing the classical fourth-order Runge–Kutta method in combination with an adaptive step-size routine. This adaptive algorithm is implemented to significantly reduce the calculation

time and ensure that the error remains within the limit of $\varepsilon = 10^{-6}$. We have confirmed the numerical convergence of our approach.

3. Results and Discussion

3.1. Valley-Asymmetry Parameter in tBLG and MLG

Lightwave-controlled valley-selective excitation in tBLG is verified by our numerical simulation. The vector potential of the CRB field is expressed as

$$A(t) = \frac{A_0 f(t)}{\sqrt{2}} \left(\left[\cos(\omega t + \phi) + \frac{R}{2} \cos(2\omega t) \right] \hat{\mathbf{e}}_x + \left[\sin(\omega t + \phi) - \frac{R}{2} \sin(2\omega t) \right] \hat{\mathbf{e}}_y \right), \quad (7)$$

where $A_0 = F_\omega / \omega$ is the amplitude of vector potential for the fundamental light field, $F_\omega = 15\,\mathrm{MW/cm^2}$ is the strength of the fundamental field, $f(t) = \exp\left(-2\ln 2 \left(\frac{t}{t_d} \right)^2 \right)$ is the envelope of the optical field, basis vectors $\hat{\mathbf{e}}_x$ and $\hat{\mathbf{e}}_y$ are two orthogonal unit vectors, and ω is the fundamental frequency. ϕ is the phase difference between two fields, which is measured in degrees throughout this work. $R = 2$ is the ratio of the doubled and fundamental frequency electric field strengths ($2\omega{:}\omega$).

The first BZ is divided into two triangular regions centered on K_1 and K_2, as shown in Figure 1a. We define the valley-asymmetry parameter to quantify valley-selective polarization as [4]

$$\eta = \frac{n_c^1 - n_c^2}{(n_c^1 + n_c^2)/2}, \quad (8)$$

where n_c^1 and n_c^2 are the residual electron populations of total conduction bands in the K_1 and K_2 valleys, respectively, at the end of the laser pulse. The residual conduction band population $n_c^{1,2}$ is obtained by integrating all the lower-triangular diagonal elements of the density matrix in the Bloch gauge $\sum_{c \in \mathrm{CB}} \rho_{cc}^{(H)}(\mathbf{k})$ delineated by $\mathbf{k}$.

Figure 2 illustrates the valley-asymmetry parameter (η) in tBLG (Figure 2a) and MLG (Figure 2b) as a function of the two-color phase (ϕ), with the fundamental wavelength set to 6000 nm. The temporal duration of the pulse is varied, using a single cycle (blue solid), three cycles (red dashed), and five cycles (yellow dotted). Clearly, for both MLG and tBLG, the valley asymmetry parameter exhibits a modulation as a function of phase, with a modulation periodicity of $180°$. Additionally, tBLG can achieve the same level of valley asymmetry when excited by a single-cycle 6000 nm CRB pulse. This phase-dependent periodicity is consistent with MLG, as expected. The specific phase for extreme valley asymmetry is determined by the interplay between the vector potential and band structure. The valley-asymmetry parameter reaches its maximum at $\phi = 16°$, $106°$, corresponding to the relative position of the CRB vector potential and the K_1 and K_2 valleys in Figure 1b,c, and there is no valley selectivity at $\phi = 61°$. Comparing Figure 2a,b, the valley asymmetry in tBLG exhibits a substantial decrease as the duration increases, whereas in MLG, it remains nearly constant or even increases slightly. To elucidate the underlying mechanism of this attenuation, we examine the time-dependent asymmetry, which is obtained from the density matrix equation at each time step. As shown in Figure 2c, the valley asymmetry in tBLG experiences a sharp decline after reaching its maximum. Notably, due to the fact that the maximum η of tBLG is almost unaffected by the pulse duration, the valley asymmetry at the end of the pulse related only to the decreased amplitude in the fallback process. Therefore, it is suggested that the longer the duration, the lower the asymmetry. Turning to the case of MLG, the asymmetry starts to increase abruptly when the optical peak field approaches its maximum, and then remains stable after reaching the peak, as shown in Figure 2d. This behavior of tBLG is markedly distinct from that of MLG.
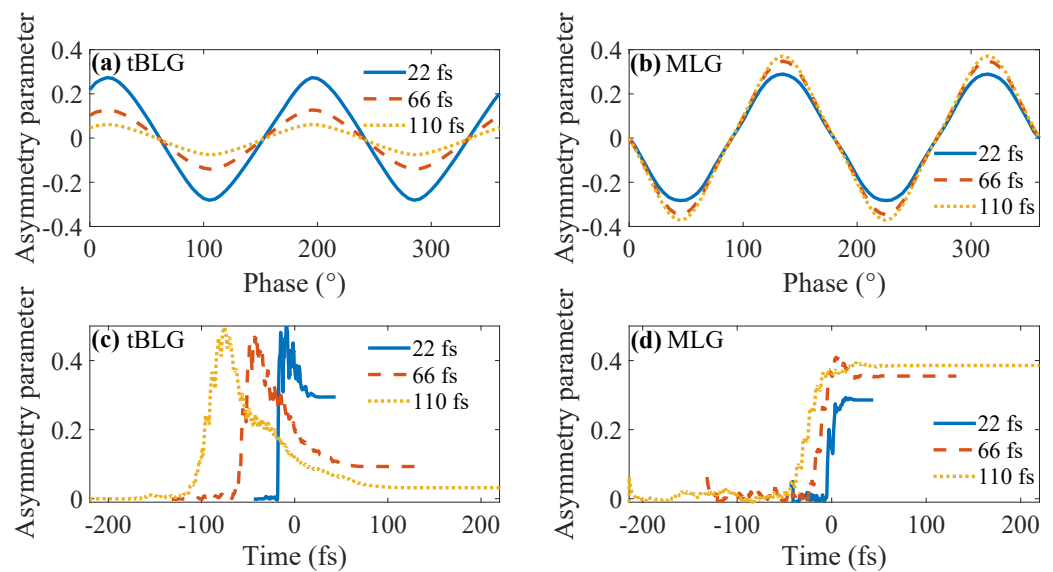
Figure 2. The valley–asymmetry parameter, denoted as η, as a function of the two-color phase in tBLG and MLG, illustrated in (**a**,**b**), respectively; and the asymmetry in (**c**) tBLG and (**d**) MLG over time, where the durations are set to 22 fs (blue solid), 66 fs (red dashed), and 110 fs (yellow dotted).

Because valley asymmetry is directly determined by population, the populations of the K_1 and K_2 valleys are first investigated as shown in Figure 3a,b. Obviously, the population of an individual valley increases monotonically with time (Figure 3a), and the population difference between the two valleys has a similar decline process to η (Figure 3b), which is independent of duration. To reveal the underlying physics for the attenuation of valley asymmetry in tBLG, it is necessary to focus on the interlayer coupling. The valley asymmetry of uncoupled tBLG (blue solid line) is calculated and compared with that of conventional tBLG (red dashed line) and MLG (yellow dotted line) (Figure 3c). All the laser parameters are kept the same as those in Figure 2a. Figure 3c indicates that the valley asymmetry of tBLG and uncoupled tBLG almost entirely overlap while increasing, implying that the interlayer interaction has no effect on asymmetry formation in the early stage. However, the valley asymmetry in the coupled tBLG begins to exhibit a decreasing trend within a time interval near to zero. Meanwhile, when all interlayer hopping is switched off, η remains almost stable after reaching its maximum, which is extremely similar to the behavior of MLG. Evidently, the decay of the valley asymmetry in tBLG disappears when the interlayer interaction is artificially set to zero, even if the twisted angle still exists.
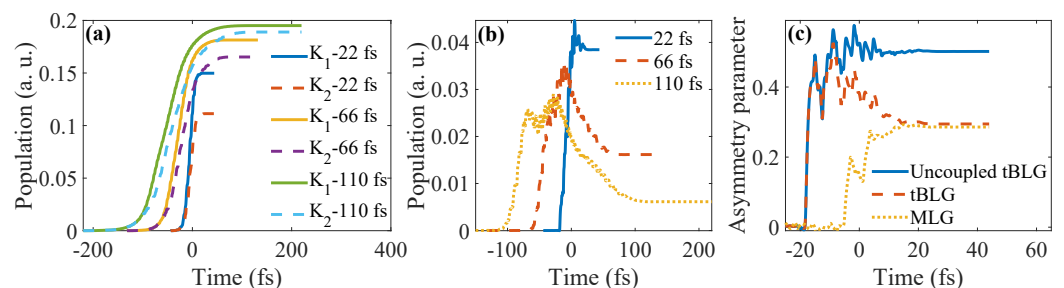
Figure 3. (**a**) The time—dependent population of K_1 (solid line) and K_2 (dashed line) valleys in tBLG, which is driven by CRB fields with durations of 22 fs, 66 fs and 110 fs. (**b**) The population difference between K_1 and K_2 valleys as a function of time. The durations of the driving light field are 22 fs (blue solid line), 66 fs (red dashed line) and 110 fs (yellow dotted line). (**c**) The valley asymmetry over time in uncoupled tBLG (blue solid line), coupled tBLG (red dashed line) and MLG (yellow dotted line); the fundamental wavelength of the drive field is 6000 nm and the pulse duration is set to 22 fs.

### 3.2. HHG Analysis and Valley Pseudospin Measurement

The interaction between light and tBLG results in valley polarization and harmonic generation at the same time. Considering the measurement issue of valley dynamics in experiments, this microscopic phenomenon can be characterized by numerical simulation of the harmonic spectrum. We give a thorough investigation of the harmonics induced by a light field with durations of 22 fs (Figure 4) and 110 fs (Figure 5), the two-color phase of 16°, and other parameters identical to those in Figure 2. Figures 4a and 5a illustrate a polarization-resolved high-harmonic spectrum, including left-handed (blue solid), right-handed (red solid) circular polarization, and total (yellow dashed) harmonic spectrum. The $(3n + 1)$ harmonics follow the polarization of the ω pulse, which is left-handed circular polarization, while the $(3n + 2)$ harmonics share the same polarization as the 2ω pulse, which is right-handed. However, $3n$ harmonics are absent on account of spin-angular momentum conservation, which has already been observed in gas high harmonics [44]. The fourth and fifth harmonic spectra excited by short (22 fs) and long (110 fs) pulses as a function of the two-color phase are depicted in Figure 4b–g and Figure 5b–d, respectively. Due to the low discreteness of harmonics driven by a single-cycle pulse (22 fs), we separate H4 and H5 from the spectrum according to the polarization state. It can be found that the harmonic yield in a single valley has the same modulation period as BZ valley asymmetry. Hence, the ϕ-dependent valley pseudospin can be measured by the harmonic yield ratio H5/H4. As shown in Figure 6, the harmonics ratio is oscillating with the same periodicity of 90° as a function of the relative phase ϕ. For the harmonics generated from the K_1 or K_2 valleys, the periodicity is 180°, which is consistent with MLG [4]. Meanwhile, reversing the helicities of the fundamental and its second harmonic simultaneously, i.e., right-handed circular ω field and left-handed circular 2ω field, does not change the conclusions from Figure 4 and Figure 5. As a result, the valley excitation and harmonic emission can be argued to be independent of the rotation of the driving pulse. Therefore, valley-selective excitation in tBLG is feasible and observable. This could be beneficial in valleytronic devices for information transfer.
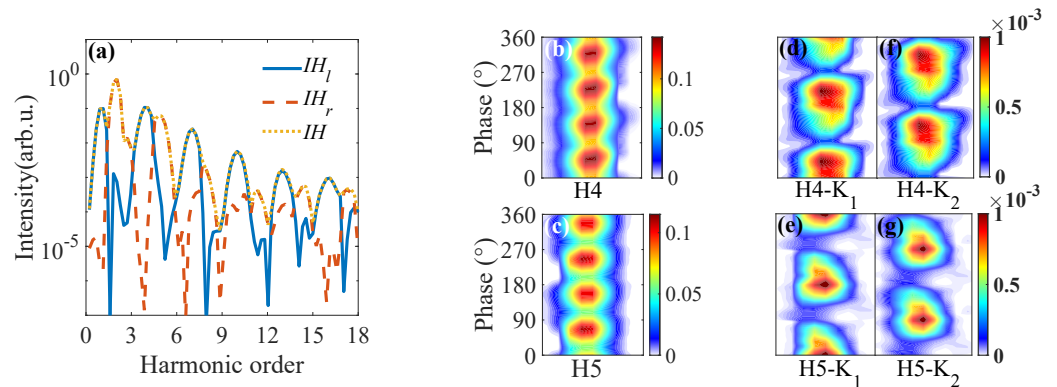

Figure 4. (**a**) The harmonic spectrum with circular polarization, including left—handed (blue solid), right—handed (red solid), and total emission (yellow dashed); the duration of the fundamental field is set to 22 fs. In addition, the fourth and fifth harmonic spectra from the BZ, K_1 valley and K_2 valley are shown as a function of the two-color phase, where (**b**–**f**) correspond to the fourth harmonic, (**c**–**g**) correspond to the fifth harmonic, and (**b**,**c**) correspond to the BZ, (**d**,**e**) correspond to the K_1 valley, and (**f**,**g**) correspond to the K_2 valley.

Incidentally, the field ratio and wavelength of CRB are also crucial in manipulating the dynamics of valley asymmetry. Here, we investigate the effect of field ratio R by calculating the valley asymmetry as a function of the two-color phase for $R = 0.5, 0.707, 2$ and 4, as shown in Figure 7a. Because R directly determines the geometry of the driving field, the CRB laser field with $R = 2$ can destroy the spatial inversion symmetry of tBLG to a significant extent, resulting in great valley-selective excitation. Figure 7b is the time-dependent asymmetry for a variable fundamental wavelength: purple dash-dotted line

for 6000 nm, yellow dotted line for 3000 nm, red dashed line for 1600 nm, and blue solid line for 800 nm. For all these wavelengths, the valley asymmetry begins to climb in an early stage of the pulse, reaches a maximum, and then decreases and finally converges to a constant value. By comparing the converged values of valley asymmetry, it can be found that the longer the wavelength, the larger the valley asymmetry. Thus, it is preferential to use a long wavelength pulse in valley-sensitive excitations.
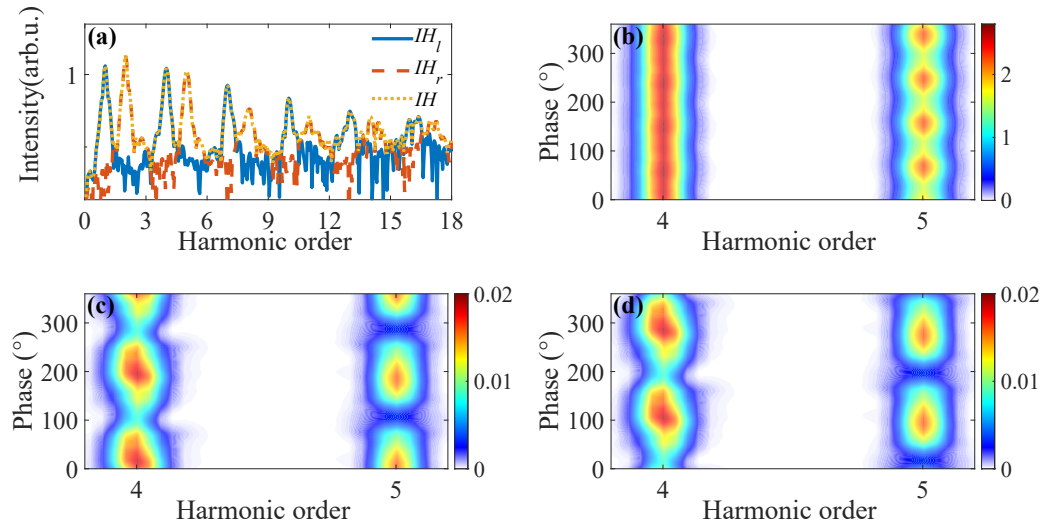
Figure 5. (**a**) The harmonic spectrum for left—handed (blue solid), right—handed (red solid) circular polarization and total (yellow dashed) emissions driven by CRB with duration of 110 fs. (**b**–**d**) The fourth and fifth harmonic spectrum for (**b**) BZ, (**c**) K_1 and (**d**) K_2 valley as a function of ϕ.
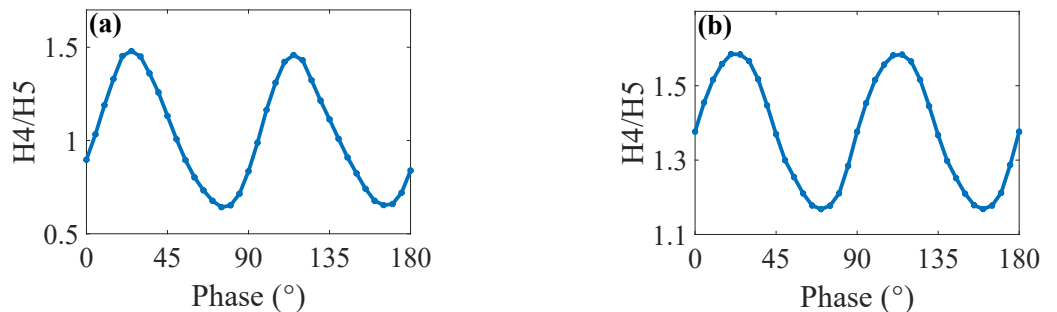
Figure 6. The harmonic yield ratio H4/H5 with durations of (**a**) 22 fs and (**b**) 110 fs in tBLG as a function of ϕ.
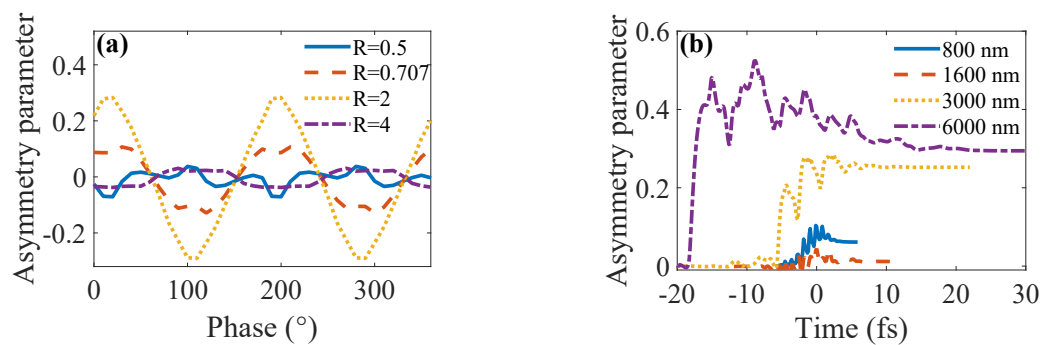
Figure 7. (**a**) ϕ—dependent valley asymmetry parameter is excited by CRB with $R = 0.5$ (blue solid), 0.707 (red dashed), 2 (yellow dotted) and 4 (purple dashed-dotted). (**b**) Valley—selective polarization is driven by CRB with fundamental wavelengths of 800 nm (blue solid), 1600 nm (red dashed), 3000 nm (yellow dotted) and 6000 nm (purple dashed—dotted).

4. Conclusions

In this study, we have conducted a theoretical investigation into lightwave-controlled valley-selective excitation in the minimal commensurate tBLG. The electron dynamics are obtained by numerically solving the time-dependent density matrix equation in the length gauge and under the tight-binding approxamation.

On the basis of the study performed, we can draw the conclusion that the sub-periodic (with respect to fundamental pulse) valley dynamics in tBLG can be effectively manipulated by a CRB light field via the two-color phase. In contrast to MLG, the valley selectivity of tBLG is notably modified by its interlayer coupling, resulting in a high sensitivity to duration. Additionally, the valley asymmetry reaches its maximum when the tBLG is illuminated with a single-cycle pulse. What is more, the valley selectivity can be conveniently measured using the intensity ratio of the fourth and fifth harmonic signals.

These findings provide a new insight into the control of valley dynamics in tBLG using CRB fields, and offer a promising avenue for the development of valleytronics based on tBLG.

Author Contributions: Conceptualization, J.C. and C.L.; methodology, J.C. and C.L.; software, J.C. and C.L.; validation, J.C.; formal analysis, J.C. and C.L.; investigation, J.C.; resources, C.L. and R.L.; data curation, J.C.; writing—original draft preparation, J.C.; writing—review and editing, J.C.; visualization, J.C. and C.L.; supervision, C.L. and R.L.; project administration, C.L. and R.L.; funding acquisition, C.L. and R.L. All authors have read and agreed to the published version of the manuscript.

Institutional Review Board Statement: Not applicable.

Informed Consent Statement: Not applicable.

Data Availability Statement: The data supporting the findings of this study are available from the corresponding author upon reasonable request.

Conflicts of Interest: The authors declare no conflicts of interest.

References

1. Lazenka, V.; Lorenz, M.; Modarresi, H.; Bisht, M.; Rüffer, R.; Bonholzer, M.; Grundmann, M.; Van Bael, M.J.; Vantomme, A.; Temst, K. Magnetic spin structure and magnetoelectric coupling in BiFeO3-BaTiO3 multilayer. *Appl. Phys. Lett.* **2015**, *106*, 082904. [CrossRef]
2. Fan, Y.; Finley, J.; Han, J.; Holtz, M.E.; Quarterman, P.; Zhang, P.; Safi, T.S.; Hou, J.T.; Grutter, A.J.; Liu, L. Resonant Spin Transmission Mediated by Magnons in a Magnetic Insulator Multilayer Structure. *Adv. Mater.* **2021**, *33*, 2008555. [CrossRef] [PubMed]
3. Hirohata, A.; Yamada, K.; Nakatani, Y.; Prejbeanu, I.L.; Diény, B.; Pirro, P.; Hillebrands, B. Review on spintronics: Principles and device applications. *J. Magn. Magn. Mater.* **2020**, *509*, 166711. [CrossRef]
4. Mrudul, M.S.; Jiménez-Galán, Á.; Ivanov, M.; Dixit, G. Light-induced valleytronics in pristine graphene. *Optica* **2021**, *8*, 422–427. [CrossRef]
5. Chen, F.; Lv, Q.; Xia, Y.; Mao, S.; Fu, L.; Zhao, S. Two-dimensional bilayer MoS2 flakes with variable size of the upper layer grown by chemical vapor deposition. *Micro Nanostruct.* **2022**, *169*, 207358. [CrossRef]
6. Selhorst, R.; Yu, Z.; Moore, D.; Jiang, J.; Susner, M.A.; Glavin, N.R.; Pachter, R.; Terrones, M.; Maruyama, B.; Rao, R. Precision Modification of Monolayer Transition Metal Dichalcogenides via Environmental E-Beam Patterning. *ACS Nano* **2023**, *17*, 2958–2967. [CrossRef]
7. Tchoumakov, S.; Bujnowski, B.; Noky, J.; Gooth, J.; Grushin, A.G.; Cayssol, J. Conservation of chirality at a junction between two Weyl semimetals. *Phys. Rev. B* **2021**, *104*, 125308. [CrossRef]
8. Huang, Z.M.; Zhou, J.; Shen, S.Q. Topological responses from chiral anomaly in multi-Weyl semimetals. *Phys. Rev. B* **2017**, *96*, 085201. [CrossRef]
9. Wu, M.M.; Sun, Y.; Li, J.; Zhao, H.; Pan, H. Valley-dependent electron scattering in Weyl semimetals. *Solid State Commun.* **2021**, *334-335*, 114387. [CrossRef]
10. Schaibley, J.R.; Yu, H.; Clark, G.; Rivera, P.; Ross, J.S.; Seyler, K.L.; Yao, W.; Xu, X. Valleytronics in 2D materials. *Nat. Rev. Mater.* **2016**, *1*, 16055. [CrossRef]

11. He, Y.L.; Guo, J.; Gao, F.Y.; Liu, X.S. Dynamical symmetry and valley-selective circularly polarized high-harmonic generation in monolayer molybdenum disulfide. *Phys. Rev. B* **2022**, *105*, 024305. [CrossRef]

12. Nakagahara, K.; Wakabayashi, K. Enhanced valley polarization of graphene on *h*-BN under circularly polarized light irradiation. *Phys. Rev. B* **2022**, *106*, 075403. [CrossRef]

13. Hung, C.M.; Dang, D.T.X.; Chanda, A.; Detellem, D.; Alzahrani, N.; Kapuruge, N.; Pham, Y.T.H.; Liu, M.; Zhou, D.; Gutierrez, H.R.; et al. Enhanced Magnetism and Anomalous Hall Transport through Two-Dimensional Tungsten Disulfide Interfaces. *Nanomaterials* **2023**, *13*, 771. [CrossRef] [PubMed]

14. Xu, Y.; Fang, Y.; Jin, G. Valley-polarized and supercollimated electronic transport in an 8-Pmmn borophene superlattice. *New J. Phys.* **2023**, *25*, 013020. [CrossRef]

15. Norden, T.; Zhao, C.; Zhang, P.; Sabirianov, R.; Petrou, A.; Zeng, H. Giant valley splitting in monolayer WS2 by magnetic proximity effect. *Nat. Commun.* **2019**, *10*, 4163. [CrossRef]

16. Rosati, R.; Wagner, K.; Brem, S.; Perea-Causin, R.; Wietek, E.; Zipfel, J.; Ziegler, J.D.; Selig, M.; Taniguchi, T.; Watanabe, K.; et al. Temporal Evolution of Low-Temperature Phonon Sidebands in Transition Metal Dichalcogenides. *ACS Photonics* **2020**, *7*, 2756–2764. [CrossRef]

17. Ye, J.; Yan, T.; Niu, B.; Li, Y.; Zhang, X. Nonlinear dynamics of trions under strong optical excitation in monolayer MoSe2. *Sci. Rep.* **2018**, *8*, 2389. [CrossRef]

18. Yuan, H.; Wang, X.; Lian, B.; Zhang, H.; Fang, X.; Shen, B.; Xu, G.; Xu, Y.; Zhang, S.C.; Hwang, H.Y.; et al. Generation and electric control of spin-valley-coupled circular photogalvanic current in WSe2. *Nat. Nanotechnol.* **2014**, *9*, 851–857. [CrossRef]

19. Mak, K.F.; He, K.; Shan, J.; Heinz, T.F. Control of valley polarization in monolayer MoS2 by optical helicity. *Nat. Nanotechnol.* **2012**, *7*, 494–498. [CrossRef]

20. Vitale, S.A.; Nezich, D.; Varghese, J.O.; Kim, P.; Gedik, N.; Jarillo-Herrero, P.; Xiao, D.; Rothschild, M. Valleytronics: Opportunities, Challenges, and Paths Forward. *Small* **2018**, *14*, 1801483. [CrossRef]

21. Hashmi, A.; Yamada, S.; Yamada, A.; Yabana, K.; Otobe, T. Valley polarization control in WSe2 monolayer by a single-cycle laser pulse. *Phys. Rev. B* **2022**, *105*, 115403. [CrossRef]

22. Langer, F.; Schmid, C.P.; Schlauderer, S.; Gmitra, M.; Fabian, J.; Nagler, P.; Schueller, C.; Korn, T.; Hawkins, P.G.; Steiner, J.T.; et al. Lightwave valleytronics in a monolayer of tungsten diselenide. *Nature* **2018**, *557*, 76–80. [CrossRef]

23. Jimenez-Galan, A.; Silva, R.E.F.; Smirnova, O.; Ivanov, M. Sub-cycle valleytronics: Control of valley polarization using few-cycle linearly polarized pulses. *Optica* **2021**, *8*, 277–280. [CrossRef]

24. Motlagh, S.A.O.; Wu, J.S.; Apalkov, V.; Stockman, I.M. Femtosecond valley polarization and topological resonances in transition metal dichalcogenides. *Phys. Rev. B* **2018**, *98*, 081406. [CrossRef]

25. Motlagh, S.A.O.; Nematollahi, F.; Apalkov, V.; Stockman, I.M. Topological resonance and single-optical-cycle valley polarization in gapped graphene. *Phys. Rev. B* **2019**, *100*, 115431. [CrossRef]

26. Mrudul, M.S.; Dixit, G. Controlling valley-polarisation in graphene via tailored light pulses. *J. Phys. B At. Mol. Opt. Phys.* **2021**, *54*, 224001. [CrossRef]

27. Rana, N.; Dixit, G. All-Optical Ultrafast Valley Switching in Two-Dimensional Materials. *Phys. Rev. Appl.* **2023**, *19*, 034056. [CrossRef]

28. Heide, C.; Boolakee, T.; Higuchi, T.; Weber, H.B.; Hommelhoff, P. Interaction of carrier envelope phase-stable laser pulses with graphene: The transition from the weak-field to the strong-field regime. *New J. Phys.* **2019**, *21*, 045003. [CrossRef]

29. Stoudenmire, E.M.; Schwab, D.J. Supervised Learning with Quantum-Inspired Tensor Networks. *arXiv* **2017**, arXiv:stat.ML/1605.05775.

30. Flouris, K.; Mendoza Jimenez, M.; Debus, J.D.; Herrmann, H.J. Confining massless Dirac particles in two-dimensional curved space. *Phys. Rev. B* **2018**, *98*, 155419. [CrossRef]

31. Kristinsson, K.; Kibis, O.V.; Morina, S.; Shelykh, I.A. Control of electronic transport in graphene by electromagnetic dressing. *Sci. Rep.* **2016**, *6*, 20082 . [CrossRef] [PubMed]

32. Tseluikin, V.; Dzhumieva, A.; Tikhonov, D.; Yakovlev, A.; Strilets, A.; Tribis, A.; Lopukhova, M. Pulsed Electrodeposition and Properties of Nickel-Based Composite Coatings Modified with Graphene Oxide. *Coatings* **2022**, *12*, 656. [CrossRef]

33. Li, X.; Shen, Q.; Zhang, Y.; Wang, L.; Nie, C. Wear behavior of electrodeposited nickel/graphene composite coating. *Diam. Relat. Mater.* **2021**, *119*, 108589. [CrossRef]

34. Sboychakov, A.O.; Rakhmanov, A.L.; Rozhkov, A.V.; Nori, F. Electronic spectrum of twisted bilayer graphene. *Phys. Rev. B* **2015**, *92*, 075402. [CrossRef]

35. Lee, S.Y.; Duong, D.L.; Vu, Q.A.; Jin, Y.; Kim, P.; Lee, Y.H. Chemically Modulated Band Gap in Bilayer Graphene Memory Transistors with High On/Off Ratio. *ACS Nano* **2015**, *9*, 9034–9042. [CrossRef]

36. Li, S.Y.; Zhang, Y.; Ren, Y.N.; Liu, J.; Dai, X.; He, L. Experimental evidence for orbital magnetic moments generated by moire-scale current loops in twisted bilayer graphene. *Phys. Rev. B* **2020**, *102*, 121406. [CrossRef]

37. Silva, R.E.F.; Martin, F.; Ivanov, M. High harmonic generation in crystals using maximally localized Wannier functions. *Phys. Rev. B* **2019**, *100*, 195201. [CrossRef]

38. Rozhkov, A.V.; Sboychakov, A.O.; Rakhmanov, A.L.; Nori, F. Electronic properties of graphene-based bilayer systems. *Phys. Rep.* **2016**, *648*, 1–104. [CrossRef]

39. Mele, E.J. Interlayer coupling in rotationally faulted multilayer graphenes. *J. Phys. D* **2012**, *45*, 154004. [CrossRef]

40. Lopes dos Santos, J.M.B.; Peres, N.M.R.; Castro Neto, A.H. Graphene Bilayer with a Twist: Electronic Structure. *Phys. Rev. Lett.* **2007**, *99*, 256802. [CrossRef]
41. Lopes dos Santos, J.M.B.; Peres, N.M.R.; Castro Neto, A.H. Continuum model of the twisted graphene bilayer. *Phys. Rev. B* **2012**, *86*, 155449. [CrossRef]
42. Du, M.; Liu, C.; Zeng, Z.; Li, R. High-order harmonic generation from twisted bilayer graphene driven by a midinfrared laser field. *Phys. Rev. A* **2021**, *104*, 033113. [CrossRef]
43. Moon, P.; Koshino, M. Optical absorption in twisted bilayer graphene. *Phys. Rev. B* **2013**, *87*, 205404. [CrossRef]
44. Neufeld, O.; Podolsky, D.; Cohen, O. Floquet group theory and its application to selection rules in harmonic generation. *Nat. Commun.* **2019**, *10*, 405. [CrossRef] [PubMed]